Sensors & Transducers, Vol. 237, Issue 9-10, September-October 2019, pp. 129-136

www.sensorsportal.com

Sensors & Transducers

Published by IFSA Publishing, S. L., 2019
http://www.sensorsportal.com

Fusion of Digital Road Maps with Inertial Sensors and Satellite Navigation Systems Using Kalman Filter and Hidden Markov Models

[1] Hamza Sadruddin and [2] Mohamed M. Atia

[1] Department of Electronics, ECE, Carleton University, Canada
[2] Department of Systems and Computer Engineering, ECE,
Carleton University, Canada
Tel.: 613-520-2600 ex: 5779
E-mail: hamza.sadruddin@carleton.ca, mohamed.atia@carleton.ca

Received: 30 August 2019 /Accepted: 27 September 2019 /Published: 30 November 2019

Abstract: Fusion of low-cost/low-power MEMS accelerometer/gyroscope sensors with Global Navigation Satellite Systems (GNSSs) is commonly used for vehicular localization, internet of things (IoT) tracking and Location-based Services (LBS). However, robust localization in dense urban areas is challenging due to GNSS service interruptions and satellite signal blockage. To overcome this problem, this paper describes a map-aided MEMS Accelerometer/Gyroscope/GNSS sensor fusion system for enhanced localization in dense urban areas under long GNSS outages. The work applies Extended Kalman Filter (EKF) to fuse GNSS measurements with MEMS Accelerometer/Gyroscope sensors in a loosely-coupled scheme. To support longer periods of GNSS outages, an advanced curve-to-curve map-matching algorithm using Hidden-Markov Models (HMM) is developed. Map-matched data points are used as position measurement feedback to the developed Kalman Filter. The developed map-aided fusion system was tested on real-road data collected in dense downtown area under long periods of GNSS service interruptions. The map-matching results showed 100 % accuracy under noisy GNSS. The results also showed robust localization performance under several minutes of GNSS blockage. The developed system is useful for autonomous cars navigation, LBS, and IoT localization in GNSS-denied areas.

Keywords: GNSS, MEMS Accelerometer/Gyroscope, HMM and EKF.

1. Introduction

Global Navigation Satellite Systems (GNSS) are the main localization sensors used in modern electronic systems. The first operational satellite-based navigation system was the U.S. system known as "Global Positioning System (GPS)" [1]. The GPS framework has been significantly enhanced over the past two decades. According to the FAA GPS Performance Analysis Report [2], horizontal accuracy of GPS (Standard Positioning Service "SPS") is within 3.351 m with a 95 % confidence level. However, in typical environments, this accuracy is affected by several factors such as atmospheric effects, sky blockage, and receiver quality. Considering the economical consideration that requires in-car GPS/GNSS receivers to be manufactured at low cost, the error is larger in practice. GNSS technology have been significantly improved by having more satellites in the sky [3-5]. In addition, GNSS accuracy can be significantly improved using several techniques such as differential GNSS (DGNSS), Augmented GNSS,

Precise Positioning Services (PPS), or real-time kinematics (RTK). However, localization in dense urban areas is still challenging due to GNSS signals multipath or complete outage for extended periods in scenarios like tunnels and/or urban canyons. Therefore, fusion of GNSS with other sensors is a common trend that has been widely adopted.

Fusion of GNSS with self-contained dead-reckoning relative motion sensors (e.g. inertial measurement units "IMU") such as low-cost/low-power MEMS accelerometer and gyroscope [4] sensors can bridge short GNSS outages. GNSS and accelerometer/gyroscope sensors can be fused using Extended Kalman Filter (EKF) [5]. In the fusion process, the localization state transition is triggered by IMU sensors (accelerometer and gyroscopes) while GNSS measurements are used as external observations. The observations in our case is GNSS location and speed measurements. This EKF fusion scheme is known as loosely-coupled EKF.

Although the GNSS/IMU fusion provides high-rate robust localization, the localization accuracy drifts quickly under GNSS outages leading to significant drifts as illustrated in Fig. 1. In addition, under signal reflections and refractions induced by high buildings, GNSS accuracy deteriorates leading to significantly noisy positioning as can be seen in Fig. 2. To solve these accuracy and availability problems and to provide accurate uninterrupted navigation services under these challenges, the integration of digital road maps with IMU and GNSS has been recently considered [6-7].

Road maps are currently widely available in modern car systems and high-definition (HD) [8] maps are currently being developed to enable self-driving cars and automated connected vehicles [8]. In contrast to conventional maps that human normally uses to display information, HD maps are different in the level of accuracy, comprehensiveness, resolution and details. HD maps are currently being developed on a large scale as can be seen in [9]. To support automated driving technology where positioning availability in real-time is crucial, this work proposes the integration of commercially available maps with GNSS and IMU. While digital road map network [10] is used in this paper, the same concepts are applicable to HD maps.

This work is an extension to the conference paper published by the authors in [11]. In contrast to existing map-matching methods that applies open-loop point-to-curve map projection, this work uses Hidden Markov Models (HMM) as an enhanced curve-to-curve map matching technique. According to state-of-art surveys [12], HMM is known for its accuracy in complex geometry and dense topology road networks. In addition, the proposed work applies the projected map-points as measurements update (feedback) to the developed EKF in a closed-loop map-matching scheme. This closed-loop approach provides more robust and accuracy filtering under long periods of GNSS outages.

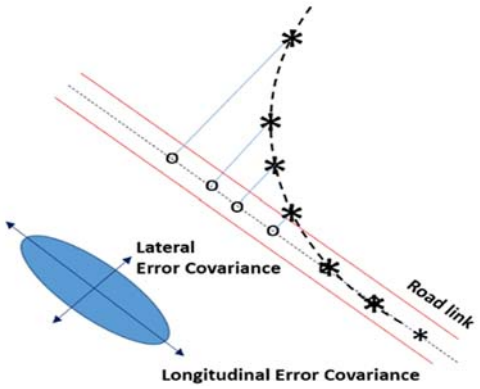

Fig. 1. Localization error reset in GNSS Outage using Road Networks Maps.

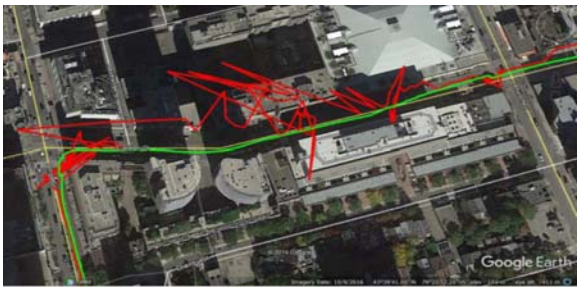

Fig. 2. NSS errors due to multipath in urban areas. Red is GNSS and green is ground-truth solution.

2. INS/GNSS Fusion System

The vehicle's kinematics can be modelled as dynamic system of states vector $x(t)$ that changes over time according to the following differential equations:

$$\dot{x}(t) = f(x(t), u(t)) + w(t), \quad (1)$$

$$y(t) = h(x(t)) + v(t), \quad (2)$$

where $f(.)$ is the nonlinear dynamic model, $w(t)$ is the stochastic system noise vector, $u(t)$ is the control signal vector, $y(t)$ is the external measurements vector, $h(.)$ is the nonlinear measurement model and $v(t)$ is the stochastic measurement noise vector. In this work, Kalman filter is adopted due to its real-time efficient performance [4-5]. However, Kalman filter works only under linear systems. Therefore, the differential equations in (1) and (2) must be linearized. Commonly, first order Taylor series expansion is used to obtain the following linearized system model:

$$\delta\dot{x}(t) = F(t)\delta x(t) + w(t), \quad (3)$$

$$\delta\dot{y}(t) = H(t)\delta x + v(t), \quad (4)$$

$$F(t) = \frac{\partial f\big(x(t), u(t)\big)}{\partial x}, \quad (5)$$

$$H(t) = \frac{\partial h(x(t))}{\partial x} \quad (6)$$

The Kalman Filter provides optimal estimation of the error state δx assuming $w(t)$ and $v(t)$ are zero-mean Gaussian noise vectors with covariance matrices defined by:

$$Q(t) = \langle w(t)w(t)^T \rangle \tag{7}$$

$$R(t) = \langle v(t)v(t)^T \rangle \tag{8}$$

and δx is the error vector with zero-mean and a covariance matrix *P* defined by:

$$P(t) = \langle \delta x(t)\delta x(t)^T \rangle \tag{9}$$

In discrete form, derivative can be approximated as follows:

$$\delta \dot{x}_k \approx \frac{\delta x_{k+1} - \delta x_k}{T}, \tag{10}$$

where T is the sampling period. To program the filtering algorithms within a digital system, Eqs. (3) and (4) can be written in discrete form as follows:

$$\delta x_k = (I + F_k T)\delta x_{k-1} + w_{k-1} \tag{11}$$

$$\delta y_k = H_k \delta x_k + v_k \tag{12}$$

The optimal estimation of the error vector,δx_k, given measurements, y_k, is calculated using two steps: prediction step

$$x_{k+1} = f(x_k, u_k) \tag{13}$$

$$P_{k+1} = (I + F_{k+1}T)P_k(I + F_{k+1}T)^T + Q_{k+1} \tag{14}$$

and update step

$$K_{k+1} = P_{k+1} H_{k+1}^T (H_{k+1} P_{k+1} H_{k+1}^T + R_{k+1})^{-1}, \tag{15}$$

$$x_{k+1} = x_{k+1} + K_{k+1}[y_{k+1} - h(x_{k+1})], \tag{16}$$

$$P_{k+1} = (I - K_{k+1}H_{k+1})P_{k+1} \tag{17}$$

In the proposed system, the vehcile's Kinematic model is used as the system model of Eq. (1) where the triggering control signal *u(t)* is the raw accelerometers and gyroscope measurements. The system states vector can be described as follows: $x_k = [p_k^{(l)}; v_k^{(l)}; \varphi_k^{lb}; b_a(t); b_\omega(t)]$, where $p_k^{(l)}$is the position vector defined in a local navigation frame l, $v_k^{(l)}$ is the velocity vector defined in local navigation frame l, φ_k^{lb} is the vehicle's orientation with respect to local-level navigation frame l, $b_a(t)$ and $b_\omega(t)$ are errors of accelerometers and gyroscope measurements respectively. For 3D rigid body kinematics, $f(.)$ is a nonlinear mapping between vehicle state and control signals at time t and the vehicle's state in the next instant of time $t + \delta t$. For a rigid body in 3D, the differential equations that describes $f(.)$ is given by [5]:

$$\dot{p}^{(l)}(t) = v^{(l)}(t) \tag{18}$$

$$\dot{v}^{(l)}(t) = R_b^l(t)\left(a^{(l)}(t) - b_a(t)\right) + g^{(l)}(t) - \left(\omega_{EL}^{(l)} + 2\omega_{IE}^{(l)}\right)v^{(l)}(t) \tag{19}$$

$$\dot{R}_b^l(t) = R_b^l(t)\left(\left[\omega^{(b)}(t) - b_\omega(t)\right] - \left[\omega_{EL}^{(l)} + \omega_{IE}^{(l)}\right]\right) \tag{20}$$

$\dot{R}_b^l(t)$ here is the direction cosine matrix that represents the vehicle's orientation. Rearding accelerometer and gyroscope errors, they are modeled using a Gauss-Markov random process as follows:

$$\dot{b}_a(t) = -\beta_a b_a(t) + \sqrt{2\sigma_a^2\beta_a}w(t), \tag{21}$$

$$\dot{b}_\omega(t) = -\beta_\omega b_\omega(t) + \sqrt{2\sigma_\omega^2\beta_\omega}w(t), \tag{22}$$

where ${\beta_a}^{-1}$, ${\beta_\omega}^{-1}$, σ_a^2 and σ_ω^2 are the time constants and covariates of Gauss-Markov process [5] [5] models of accelerometer and gyroscopes biases respectively. $\dot{R}_b^l(t)$ is the trigonometric function of the vehicle's Euler angles vector$\varphi^{lb}(t)$ defined as 3×3 matrix:

$$R_b^l(t) = \begin{bmatrix} c_{11} & c_{12} & c_{13} \\ c_{21} & c_{22} & c_{23} \\ c_{31} & c_{32} & c_{33} \end{bmatrix}, \tag{23}$$

where

$$\begin{aligned} c_{11} &= \cos\theta\cos\psi \\ c_{12} &= -\cos\phi\cos\psi + \sin\phi\sin\theta\cos\psi \\ c_{13} &= \sin\phi\sin\psi + \cos\phi\sin\theta\cos\psi \\ c_{21} &= \cos\theta\sin\psi \\ c_{22} &= \cos\phi\cos\theta + \sin\phi\sin\theta\sin\psi \\ c_{23} &= -\sin\phi\cos\psi + \cos\phi\sin\theta\sin\psi \\ c_{31} &= -\sin\theta \\ c_{32} &= \sin\phi\cos\theta \\ c_{33} &= \cos\phi\cos\theta \end{aligned} \tag{24}$$

$\omega_{EL}^{(l)}$ is the rotation rate of the local-level navigation frame l with respect to the earth frame due to motion of the vehicle on the ellipsoid surface of Earth and $\omega_{IE}^{(l)}$ is the rotation rate of earth frame with respect to the imaginary non-rotating inertial navigation frame due to Earth's rotation.

To avoid singularities and numerical instability, the direction cosine matrix $R_b^l(t)$ is converted to quaternion variable $q_b^l(t) = [q_1 q_2 q_3 q_4]^T$[9, 20] and the numerical integration is performed in the quaternion domain according to the following equation:

$$\dot{q}_b^l(t) = \frac{1}{2}q_b^l(t)\left(\left[\omega_q{}^{(b)}(t) - b_{\omega_q}(t)\right] - \left[\omega_{EL_q}^{(l)} + \omega_{IE_q}^{(l)}\right]\right) \tag{25}$$

In Eq. (25), ${\omega_q}^{(b)}$, $b_{\omega_q}(t)$, $\omega_{EL_q}^{(l)}$, and $\omega_{IE_q}^{(l)}$ are the gyroscope measurements, gyroscope biases, transport rate, and earth rate vectors in quaternion vector form. In the quaternion domain, the orientation state equation is linear as shown in Eq. (10) instead of the trigonometric functions used in $R_b^l(t)$. The calculated quaternion states are then transformed back direction cosine matrix $R_b^l(t)$ as follows:

$$R_b^l(t) = \begin{bmatrix} q_1^2+q_2^2+q_3^2+q_4^2 & 2(q_2q_3-q_1q_4) & 2(q_2q_4-q_1q_3) \\ 2(q_2q_3+q_1q_4) & q_1^2-q_2^2+q_3^2-q_4^2 & 2(q_3q_4-q_1q_2) \\ 2(q_2q_4+q_1q_3) & 2(q_3q_4+q_1q_2) & q_1^2-q_2^2-q_3^2+q_4^2 \end{bmatrix} \quad (26)$$

The Kalman filter receives updates from GNSS position and velocity and map-matched position. Therefore, the measurement model is defined as follows:

$$\begin{bmatrix} p_{k+1}^{(l)}\big|_{GNSS\,(or\,map)} - p_{k+1}^{(l)}\big|_{INS} \\ v_{k+1}^{(l)}\big|_{GNSS} - v_{k+1}^{(l)}\big|_{INS} \end{bmatrix} = H\delta x_{k+1}, \quad (27)$$

where H is defined accordingly. The measurement noise covariance matrix (the R matrix) for GNSS measurements updates is given by:

$$R_{6x6} = \begin{bmatrix} \Sigma_{3x3}^{gnss\_pos} & O_{3x3} \\ O_{3x3} & \Sigma_{3x3}^{gnss\_vel} \end{bmatrix} \quad (28)$$

The measurement noise covariance matrix (the R matrix) for map-positions updates is given by:

$$R_{3x3} = \Sigma_{3x3}^{map\_pos} \quad (29)$$

where 0_{3x3} is the 3 by 3 zeros matrix, $\Sigma_{3x3}^{gnss_pos}$is the 3×3 diagonal matrix which represents GNSS position error covariance, $\Sigma_{3x3}^{gnss\_vel}$ is the 3×3 diagonal matrix which represents GNSS velocity error covariance, and $\Sigma_{3x3}^{map\_pos}$ is the 3×3 diagonal matrix that represents error covariance matrix for map-matched position. The design matrix H is given by:

$$H = \begin{bmatrix} I_{3x3} & 0_{3x3} & 0_{3x9} \\ 0_{3x3} & I_{3x3} & 0_{3x9} \end{bmatrix} \quad (30)$$

3. Enhanced Performance via Map-Matching

Localization errors due to GNSS multipath and IMU drifts can be reduced by map-matching and by using the projected position on road map links to reset localization errors as can be seen Fig. 3. This technique is called map-matching (MM)-feedback which greatly enhances the accuracy as seen in Fig. 2. In Fig. 1, map-matching enhances the error covariance in the lateral direction of the moving object. In Fig. 3, map-matching enhances localization error covariance in both lateral and longitudinal directions of the moving platform. In this work, an enhanced curve-to-curve map-matching algorithms using Hidden-Markov Models (HMM) is described.

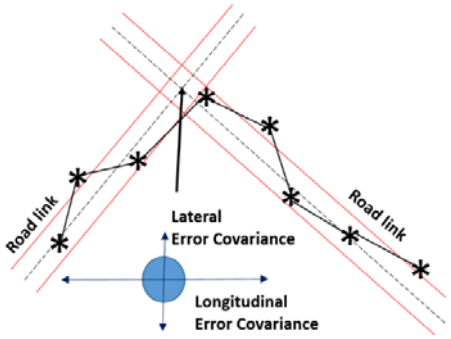

Fig. 3. Map-matching improved accuracy in GNSS outage.

3.1. Hidden Markov Models (HMM)

HMMs framework has been widely used to model random processes that are going through a series of hidden states and generating noisy observables. A Markov model is a stochastic model that describes the observations of a sequence of states $S = [s(1), s(2), s(3)\ldots., s(N)]$, where $s(k)$ depends only on $s(k-1)$. Under this assumption, the series of sequence (S) is called a Markov Process [13]. The transition from state $s(k-1)$ to state $s(k)$ is modeled by a conditional transition probability given by:

$$a_{ij} = p\big(s(k) = S_i | s(k-1) = S_j\big) \quad (31)$$

This conditional transition probability forms a Markov model. The probability of any observed sequence under a certain Markov Process and Markov model M is given by:

$$p(s(1), s(2), s(3)\ldots., s(N)|M) = p\big(s(1)\big)\prod_{i=1}^{N-1} p\big(s(i+1)|s(i)\big) \quad (32)$$

If the states are not directly measurable (hidden) but can be indirectly observed through a sequence of outputs $\{x(1), x(2), x(3)\ldots., x(N)\}$, the process is called a Hidden Markov Process. An illustrative diagram of HMM is shown in Fig. 4. The HMM in this case is characterized by the transition probability and an emission probability that represents the probability that a given state $s(k)$ generates an output$x(k)$:

$$p\big(s(k) \to x(k)\big)$$

given a sequence of outputs, HMM can estimate the most probable sequence of states $\{x(1), x(2), x(3)\ldots., x(N)\}$, that explains the observed outputs. This problem is solved by selecting the sequence of states that maximizes the HMM probability as follows:

$$\bar{S} = argmax_{S\in\{s(1),s(2),\ldots s(N)\}} \begin{bmatrix} p(s(1)\rightarrow x(1))\prod_{i=1}^{N-1} p(s(i+1)|s(i)) \\ p(s(i+1)\rightarrow x(i+1)) \end{bmatrix} \quad (33)$$

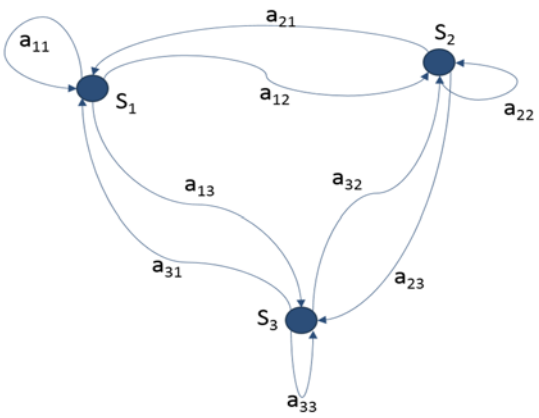

Fig. 4. Markov Process Diagram.

HMM estimation method is called "decoding" and it is solved using the Viterbi Algorithm [14]. In the proposed system, the hidden states represent map links and the observable outputs are the vehicle poses. To develop a robust map-matching framework, the vehicle pose history, roads geometry, and map topology constraints must be considered. Therefore, the emission and transition probabilities of a HMM are formulated such that they reflect all the aforementioned constraints. The HMM-based framework is illustrated in Fig. 5. The emission probabilities are calculated as follows:

$$s_{il} = \frac{w_{il}}{\sum_{k\in M_i} w_{ik}}, \quad (34)$$

where M_i is the set of all map segments within 50 m distance from current vehicle position in the i^{th} epoch. The weighting parameter w_{il} is calculated as follows:

$$w_{il} = Ae^{-aD_{il}} + Be^{-b\|\Delta A\|^2}, \quad (35)$$

where $D_{il}$is the distance from the vehicle's estimated position in the i^{th} epoch and its projection on the l^{th} map segment. ΔA_{il} is the normalized angle difference between the vehicle's estimated heading in the i^{th} epoch and the heading of the l^{th} map segment. The parameters A, a, B, and b are constants chosen to achieve balanced weighting that considers both distance and direction of motion consistency. The transition probabilities are calculated as follows:

$$a_{lm}^{ij} = \frac{w_{lm}^{ij}}{\sum_{k\in L_l} w_{lk}^{ij}}, \quad (36)$$

where a_{lm}^{ij} is the probability of transition from l^{th} map link to m^{th} map link given the vehicle' position at epochs i and j respectively. $L_l$is the set of all map links connected to l^{th} map link. The weighting parameter w_{lm}^{ij} is calculated as follows

$$w_{lm}^{ij} = C_{lm}e^{-c\|\Delta A_{ij}-\Delta A_{lm}\|}, \quad (37)$$

where ΔA_{ij} is the normalized angle difference between the vehicle's estimated heading in the i^{th} and j^{th} epochs, ΔA_{lm} is the normalized angle difference between the heading of the l^{th} and m^{th} map segments and c_{lm} is the connectivity parameter that determines if map segments l^{th} and m^{th} are topologically connected and c is a constant parameter.

In our proposed system, the possible road network map segments were represented as hidden states, whereas the vehcile's location was an observable state. In this case, vehicle's dynamics and road network topology are used to build transition probability matrix while emission probabilities represented the probability that a given state (i.e. road segment) generates an output (vehicle's location). Fig. 3 shows how the problem is modeled as a HMM. Viterbi Algorithm [3] was used to find the sequence of road map segments that most likely to have generated the observed locations. To develop a robust map-matching framework, the vehicle location and orientation history, roads geometry, and map topology constraints were considered in calculating emission and transition probabilities. Fig. 6 shows the system components.

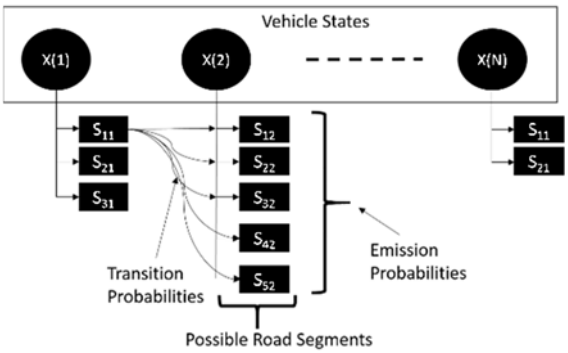

Fig. 5. Map-matching as HMM.

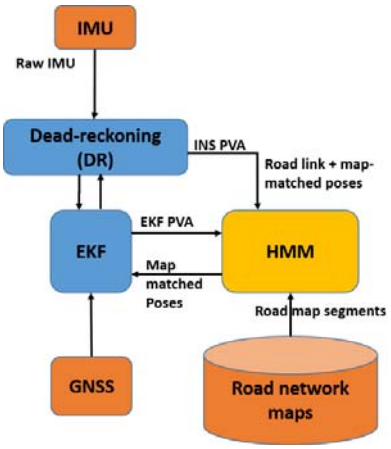

Fig. 6. Overall System Block Diagram.

4. Experimental Setup

To collect road data and test the developed HMM/EKF algorithms, an embedded system that interface with GNSS receiver and IMU has been realized on a Jetson TX2 board shown in Fig. 7. The Jetson TX2 computer is interfaced with Ublox-7 GNSS receiver and MPU 9250 IMU. Map data has been obtained from Navteq road network map data from HERE [15].

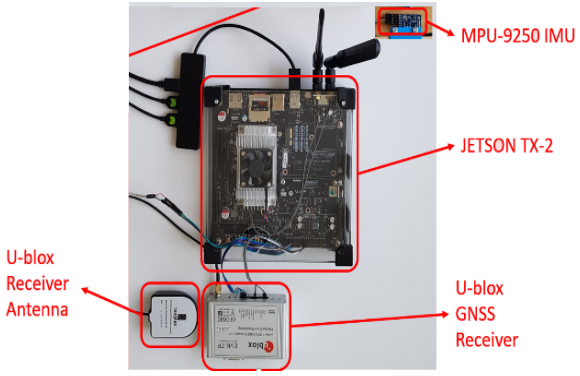

Fig. 7. The developed sensors logging platform.

A series of experiments were performed in both GNSS available and denied environments, in order to obtain and validate results. Table 1 shows the specifications of the developed sensors logger systems, whereas Fig. 8 shows an experimental car equipped by the developed logger and a ground-truth navigation system ProPak6 from Novatel [8]. All data has been synchronized using the GPS timing.

Table 1. Specifications of the data logger sensors.

Specification	Value
MPU9250 IMU	
Accelerometer technology	MEMS
Accelerometer random noise	0.0294 $(m/s^2/\sqrt{Hz})$
Gyroscope technology	MEMS
Gyroscope noise	0.01 $(°/s/\sqrt{Hz})$
U-blox 8 GNSS Receiver	
Horizontal location accuracy	2.5 m
Velocity accuracy	0.1 m/s

Fig. 8. Experimental Car.

5. Results

In this section, sample of the obtained results in downtown Toronto is demonstrated. First, to test the standalone GNSS accuracy, we run a simple static test where the Ublox GNSS calculated position is recorded and compared against the ground truth position. The test was performed in urban area but mostly open-sky. Fig. 9, Fig. 10 and Fig. 11 show the north, east, and vertical positioning accuracy respectively. As can be seen, the accuracy is consistent with the reported accuracy in the US FFA GPS accuracy report in [2]. Improving this accuracy down to sub-meter can be done with IMU fusion. However, if GNSS is blocked or severely interrupted, standalone IMU/odometery solution will drift leading to wrong map segment selection as can be seen in Fig. 12. This drift will grow without bound if not corrected by map-matching.

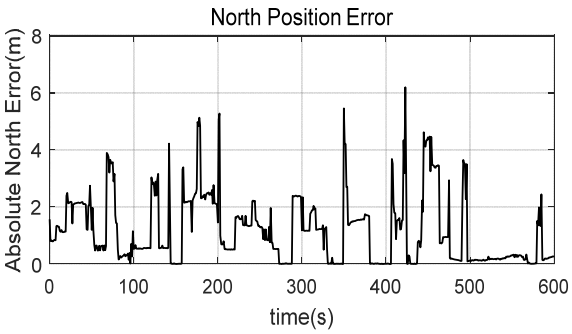

Fig. 9. Standard GPS Test (North Position Accuracy).

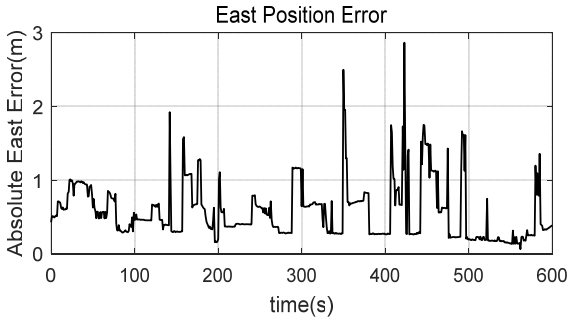

Fig. 10. Standard GPS Test (East Position Accuracy).

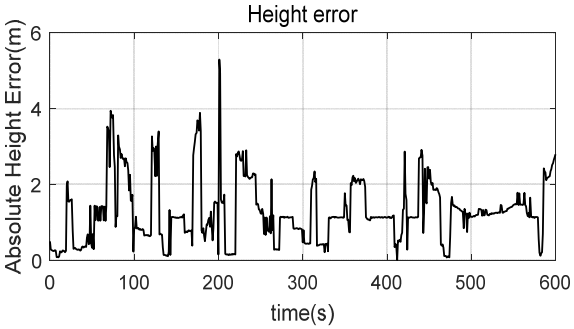

Fig. 11. Standard GPS Test (Vertical Position Accuracy).

Fig. 12. IMU/odometer solution drift leading to wrong map segment selection. The circle indicates the start of the GNSS outage, and the rectangle indicates the drift that leads to wrong map segment selection.

Fig. 13 and Fig. 14 demonstrate the benefit of the described HMM-based map-matching fusion. As can be seen in the figures, map-aided solution successfully identifies the map segment on which the vehicle is moving on.

Fig. 13. Map-matching in an intersection. Map aided solution is in yellow shows the correct track while red curves show the road map network.

Fig. 14. Map-matching in an exit. Map aided solution is in yellow shows the correct track while red curves show the road map network.

The accuracy is demonstrated under challenging road network intersection with a bridge (Fig. 13) and in a high-way exit fork (Fig. 14). Table 2 shows the localization error under four 60-seconds GNSS outages with and without the developed map-aided fusion system. During the outage, only IMU is used without any additional measurements from the car speed measurements or non-holonomic constrains.

To test long GNSS outage, a simulated GNSS outage of 20 minutes has been tested. As can be seen from Fig. 15, the system sustained reliable map-matching and enhanced accuracy for the entire 20 minutes with a sub-meter overall localization error.

Table 2. The localization error under four 60-seconds GNSS outages with and without the developed map-aided fusion system.

	2D horizontal error (m) without map-matching (IMU odometry only, no GNSS, non-holonomic constraints, no speed measurements)			
	Outage 1	**Outage 2**	**Outage 3**	**Outage 4**
RMSE	19.73	19.05	18.64	18.84
Max Error	44.61	37.34	38.44	41.21
	2D horizontal error (m) with map-matching (IMU odometry only plus HMM map feedback)			
	Outage 1	**Outage 2**	**Outage 3**	**Outage 4**
RMSE	0.65	0.79	0.45	0.69
Max Error	1.78	1.62	1.69	1.83

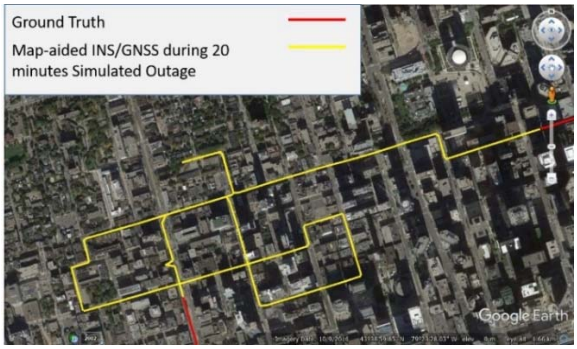

Fig. 15. Improved accuracy in long GNSS outage in Downtown area (20 minutes).

6. Conclusion

This work introduced an enhanced HMM-based map-aided IMU/GNSS sensor fusion system on an embedded platform. HMM has been shown to be a robust and accurate map-matching framework that can support continuous navigation for long periods of GNSS outages. An outage of 20 minutes has been tested with sub-meter positioning accuracy and 100 % map segment selection accuracy has been achieved.

By introducing this proposed implementation of HMM-based map-matching IMU/GNSS fusion, this work will open the door for a new generation of robust and efficient localization systems that will enable several emerging applications such as self-driving cars and internet of things. Although segment-based road network maps have been used in this work, the concept is applicable to emerging HD maps to enable self-driving cars to navigate in GNSS-denied and challenging areas.

References

[1]. P. Misra, P. Enge, Global Positioning System, Signals, Measurements, and Performance, *Ganga-Jamuna Press*, 2011.

[2]. William J. Hughes Technical Center, Global Positioning System (GPS), Standard Positioning Service (SPS), Performance Analysis Report #86, William J. Hughes Technical Center, NSTB/WAAS T&E Team, July 31, 2014.

[3]. A. El-Rabbany, Introduction to GPS: The Global Positioning System, Second Edition, *Artech House*, 2006.

[4]. J. Farrell, Aided Navigation: GPS with High Rate Sensors, *McGraw-Hill*, New York, 2008.

[5]. P. D. Groves, Principles of GNSS, Inertial, and Multisensor Integrated Navigation Systems, *Artech House*, 2013.

[6]. R. Toledo, D. Betaille, F. Peyret, J. Laneurit, Fusing GNSS, Dead-Reckoning, and Enhanced Maps for Road Vehicle Lane-Level Navigation, *IEEE Journal of Selected Topics in Signal Processing*, Vol. 3, Issue 5, 2009, pp. 798-809.

[7]. R. Toledo, D. Betaille, F. Peyret, Lane-Level Integrity Provision for Navigation and Map Matching With GNSS, Dead Reckoning, and Enhanced Maps, *IEEE Transactions on Intelligent Transportation Systems*, Vol. 11, Issue 1, 2010, pp. 100-111.

[8]. H. G. Seif, X. Hu, Autonomous Driving in the iCity—HD Maps as a Key Challenge of the Automotive Industry, *Elsevier, Engineering*, Vol. 2, Issue 2, June 2016, pp. 159-162.

[9]. S. Niijima, J. Nitta, Y. Sasaki, H. Mizoguchi, Generating 3D fundamental map by large-scale SLAM and graph-based optimization focused on road center line, in *Proceedings of the 26th IEEE International Symposium on Robot and Human Interactive Communication (RO-MAN)*, Lisbon, Portugal, September 2017.

[10]. M. M. Atia, A. R. Hilal, C. Stellings, E. Hartwell, J. Toonstra, W. B. Miners, O. A. Basir, A Low-Cost Lane-Determination System Using GNSS/IMU Fusion and HMM-Based Multistage Map Matching, *IEEE Transactions on Intelligent Transportation Systems*, Vol. 18, Issue 11, 2017, pp. 3027-3037.

[11]. H. Sadruddin, M. M. Atia, Real-time Fusion of MEMS Accelerometers/Gyroscopes with Global Navigation Satellite Systems and Road Networks for Enhanced Urban Localization, in *Proceedings of the 5th International Conference on Sensors and Electronic Instrumentation Advances (SEIA'19)*, Tenerife (Canary Islands), Spain, 25-27 September 2019, pp. 153-156.

[12]. M. R. Manikandan, Dr. R. Latha, A Literature Survey of Existing Map Matching Algorithms for Navigation Tehcnology, *International Journal of Engineering Sciences & Research Technology*, Vol. 6, Issue 9, 2017, pp. 326-331.

[13]. R. J. Elliott, L. Aggoun, J. B. Moore, Hidden Markov Models: Estimation and Control, *Springer, Business & Economics*, 1995.

[14]. L. K. Balivada, K. P. Raju, Optimization Techniques of Viterbi Algorithm: Performance Analysis of Different Algorithms, *LAP LAMBERT Academic Publishing*, 11 May 2012.

[15]. HERE, [Online], https://company.here.com/here/ [Accessed 19 January 2016].

[16]. P. G. Savage, Strapdown Analytics - Second Edition, *Strapdown Associates, Inc*., Minnesota, USA, 2000.